Distinct outcomes by dynamically encircling an exceptional point along homotopic loops

Xu-Lin Zhang,[1] Jun-Feng Song,[1] C. T. Chan,[2] and Hong-Bo Sun[1,3,*]

[1]*State Key Laboratory of Integrated Optoelectronics, College of Electronic Science and Engineering, Jilin University, Changchun 130012, China*

[2]*Department of Physics, The Hong Kong University of Science and Technology, Clear Water Bay, Hong Kong, China*

[3]*State Key Laboratory of Precision Measurement Technology and Instruments, Department of Precision Instrument, Tsinghua University, Haidian, Beijing 100084, China*

(Received 11 March 2019; published 21 June 2019)

We study a two-state non-Hermitian waveguide system that carries an exceptional point (EP). It is commonly believed that dynamically encircling an EP exhibits a chiral behavior when the starting point of the loop lies in the branch cut with eigenmodes being symmetric and antisymmetric modes. We show here that such statement is conditional; i.e., the dynamics can in fact be nonchiral for specially designed loops with the starting point in the branch cut. In particular, we find that for two homotopic loops (i.e., loops that can be transformed continuously from one to another without crossing any EP), the outcomes can be completely different even if the two loops share the same starting state, enclose the same EP, and encircle the EP in the same direction. Our findings greatly enrich the understanding of the physics in dynamical processes of EP encircling in non-Hermitian systems.

DOI: 10.1103/PhysRevA.99.063831

I. INTRODUCTION

Non-Hermitian systems have degeneracies known as exceptional points (EPs) that exhibit interesting properties [1–3] and lead to a variety of applications, such as loss induced transmission enhancement [4], sensing with enhanced sensitivity [5,6], lasing applications [7–9], asymmetric mode switching [10,11], and others [12–16]. Consider a non-Hermitian system working at its EP; any perturbation to the system will destroy the EP. In particular, when one introduces two perturbations in a parameter space, the eigenvalues of the system around the EP form self-intersecting energy sheets known as Riemann sheets [17]. The topological structure of the energy sheets around the EP has attracted considerable attention recently due to its extraordinary properties.

One of the interests related to the topological structure is the stroboscopic encircling of the EP in which the process is adiabatic [18–20]. An interesting phenomenon is that a state does not return to itself after adiabatically looping the EP. This phenomenon was demonstrated experimentally in some two-state systems such as microwave systems [18], exciton-polariton systems [19], and acoustic systems [20]. In a three-state system that possesses a third-order EP, it was predicted that a state will return to itself by looping the EP three times [21]. Quite recently, some researchers studied multistate systems and found unexpectedly that loops enclosing the same EP, starting from the same initial state and encircling the EP in the same direction, do not necessarily share the same end outcome [22,23]. The researchers introduced the topological notion of homotopy to explain the unexpected phenomenon [22]. We see that the study of stroboscopic encircling of the EP has revealed some interesting physics in non-Hermitian systems.

Another topic of current interest is the dynamical encircling of the EP, which not only can reveal alternative physics of non-Hermitian systems but also can lead to some fascinating applications unique to non-Hermitian systems [10,11,24–34]. In contrast to the stroboscopic encircling of the EP, the process of dynamical encircling was predicted to exhibit more complex dynamics since adiabaticity may break down because of the presence of non-Hermiticity [24,25]. Theories [26–28] and experiments [10,11] showed that dynamically encircling an EP exhibits chiral dynamics when the starting point of the loop lies near the branch cut [or parity-time (PT) symmetric phase]. The chiral dynamics can be applied for asymmetric mode switching [10,11]. Later, the dynamics was found to depend on the starting point of the loop; i.e., starting from the PT-broken phase can lead to nonchiral dynamics [30]. It is in fact the location of the starting point of the loop that determines the dynamics, rather than the encircling of the EP. As such, the chiral-state switching behavior was also found for loops excluding the EP, as long as the starting point lies in the branch cut (or PT-symmetric phase) and the loop is in the vicinity of the EP [31]. The dynamical processes, especially the nonadiabatic transitions which are keys to the chiral and nonchiral behavior, have been investigated using different theoretical frameworks [28,32]. There are also some investigations on the dynamical encircling of the EP in more complex systems [33,34].

Although the dynamical encircling of the EP has been studied extensively, the loops in most of the previous works have regular shapes (e.g., elliptical loops). The study of the stroboscopic encircling of homotopic loops has revealed some unique physics, where the loops are not regular loops but have unusual shapes [22,23]. This leads us to think that introducing the concept of homotopy into dynamical encircling of the EP may also lead to alternative physics and potential applications. A natural question to ask is whether the shape of the loop

*hbsun@tsinghua.edu.cn

can affect the dynamics in the EP encircling. One may also be interested in whether the conclusion found in stroboscopic encircling of the EP associated with homotopy is applicable to the case of dynamical encircling.

In this work, we address the above questions by studying a non-Hermitian system consisting of coupled waveguides. The system possesses an EP and we design two loops that are homotopic to study the dynamical encircling of the EP. Each loop has a starting and end point near the branch cut, and the dynamics would be chiral according to the conclusion of previous studies [10,11,30]. However, we show that the dynamics of each loop is nonchiral because of the specially designed shape, which indicates that the shape of the loop can also affect its dynamics. Moreover, we show that although the two loops are homotopic, their outcomes are completely different, indicating that the rules found in stroboscopic encircling of the EP associated with homotopy are not applicable to the case of dynamical encircling. We perform numerical simulations to reveal the physics and derive a theory to explain the unexpected phenomenon.

II. SYSTEM UNDER INVESTIGATION

We consider a non-Hermitian passive system consisting of a lossy waveguide and a lossless waveguide [see Fig. 1(a) for the cross section]. The waveguides are assumed to work at the optical communication wavelength (∼1550 nm), and the refractive indices of the lossy and lossless waveguides are $3.48 + 0.1i$ and 3.48, respectively. The widths of them are denoted by W_1 and W_2, and symbols H and g represent the height of the waveguides and the gap distance within. The substrate and the background are assumed to have the refractive index of 1.44 and 1, respectively. In the potential experiment, the lossless waveguide and the substrate can be made of silicon and silica, respectively. The loss in the system may be introduced by doping the waveguide with impurities. In the following study, we fix $W_1 = 600$ nm and $H = 100$ nm. Using the above parameters, we applied COMSOL [35] to calculate the effective mode index n_{eff} of the eigenmodes supported in the waveguides system as a function of W_2 and g. Figures 1(b) and 1(c) plot the real part and imaginary part of the eigenvalues, respectively. Under the system parameters, each waveguide works at the single mode condition. Therefore, the coupled system supports only two eigenmodes, and we see two self-intersecting energy sheets also known as Riemann sheets. There is an EP located at $W_2 = 591$ nm and $g = 90$ nm, at which the coupling between the two waveguides is equal to their loss difference.

Figure 2(a) shows the parameter space where the EP is marked by a red star. The red dashed curve represents the branch cut which connects the adjacent Riemann sheets. It also corresponds to the region where the imaginary parts of the eigenvalues coalesce. We consider a specially designed loop 1 which is parametrized by

$$W_2(z) = 600 + \sigma\left(100 - \frac{75z}{L}\right)\cos\left(\frac{9z}{2L}\pi - \frac{\pi}{2}\right),$$
$$g(z) = 120 + \left(100 - \frac{75z}{L}\right)\sin\left(\frac{9z}{2L}\pi - \frac{\pi}{2}\right), \quad (1)$$

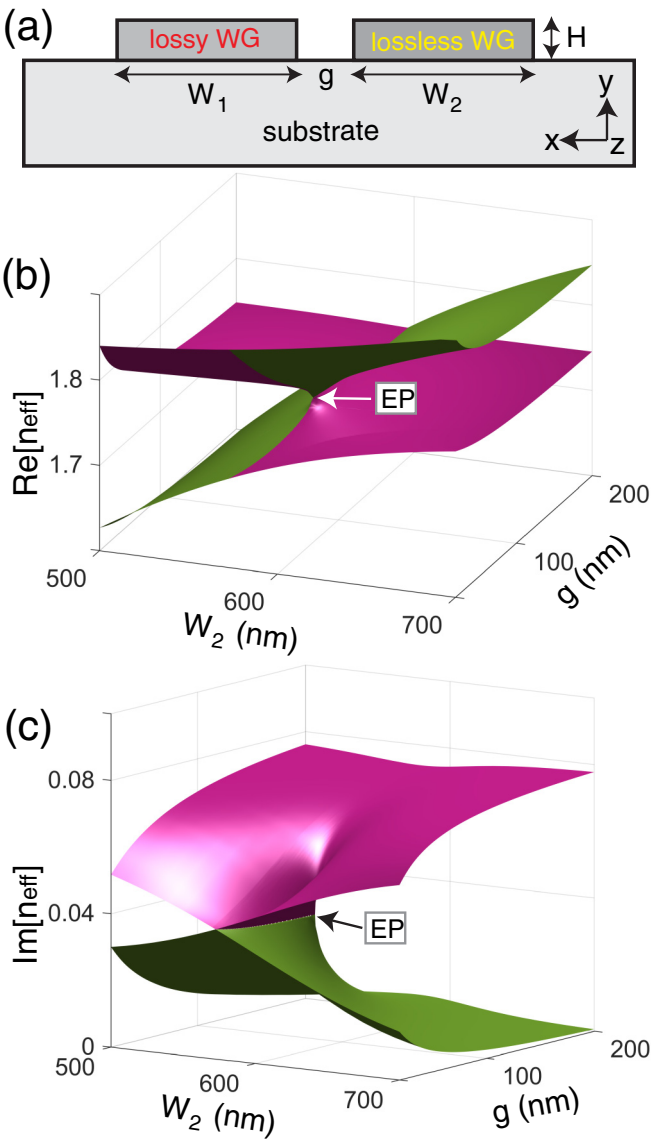

FIG. 1. (a) Cross-sectional view of a non-Hermitian system consisting of coupled waveguides, where the left waveguide is lossy and the right one is lossless. (b), (c) Calculated (b) real part and (c) imaginary part of the effective mode index of the system as a function of W_2 and g at 1550 nm. The structural parameters are $W_1 = 600$ nm and $H = 100$ nm.

when $0 \leqslant z \leqslant 2L/3$, and

$$W_2(z) = 600 + \sigma\left(\frac{150z}{L} - 50\right)\cos\left(\frac{\pi}{2} - \frac{3z}{L}\pi\right),$$
$$g(z) = 120 + \left(\frac{150z}{L} - 50\right)\sin\left(\frac{\pi}{2} - \frac{3z}{L}\pi\right), \quad (2)$$

when $2L/3 \leqslant z \leqslant L$, where L denotes the length of the system, z is ranging from 0 to L, and $\sigma = 1$. The unit of W_2 and g in the above formula is in nanometers.

Although loop 1 encloses the EP, it is different from the regular loops studied in previous works since it has a "tail" on the right-hand side of the EP. We also consider in Fig. 2(b) a loop 2 which also encircles the EP but with a tail on the

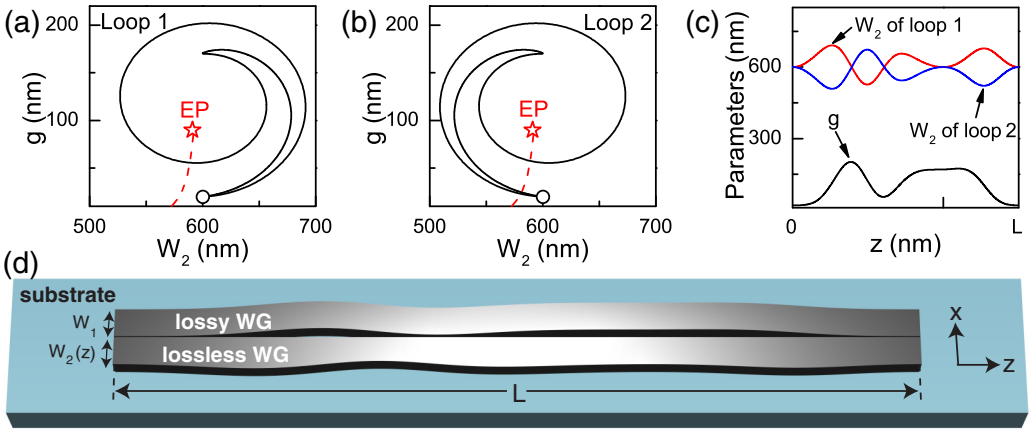

FIG. 2. (a), (b) Parameter space of the non-Hermitian system possessing an EP. (a) Loop 1 and (b) loop 2 that encircles the EP with a starting and end point (see the circle) close to the branch cut (see the red dashed curve). (c) The variation of W_2 and g along z-axis for loop 1 and loop 2. (d) Top view of the waveguides system in which the wave transmission through it is equivalent to the evolution in the parameter space following loop 1.

left-hand side of the EP. Loop 2 can also be generated by Eqs. (1) and (2) except that $\sigma = -1$. The starting point of the two loops lies at $W_2 = 600$ nm and $g = 20$ nm [see the circle in Figs. 2(a) and 2(b)], which is very close to the branch cut where the two eigenmodes share the same loss. At the starting point, one of the eigenmodes is a symmetric mode while the other one is an antisymmetric mode, with the energy almost evenly distributed in the two waveguides. Figure 2(c) shows the variations of W_2 and g as a function of z for the two loops. Taking loop 1 for example, the schematic diagram of the waveguide system is drawn in Fig. 2(d), where the wave transmission through the system is equivalent to the dynamical encircling of the EP in the parameter space following the designed loop 1. Wave propagations from the left-hand side to the right-hand side follow a counterclockwise loop while those from the right-hand side to the left-hand side travel in a clockwise loop.

In the following sections, we will use loop 1 and loop 2 to reveal some interesting physics in the proposed non-Hermitian system.

III. NONCHIRAL DYNAMICS OF SPECIALLY DESIGNED LOOPS

We study the dynamics of loop 1 in this section. Previous studies on non-Hermitian systems showed that when the starting point of a loop that encloses an EP lies near the branch cut (or PT-symmetric phase), dynamically encircling the EP exhibits a chiral transmission behavior in the sense that counterclockwise and clockwise loops result in different final states [10,11,28]. The loop 1 here obviously satisfies the above conditions, but we will show that the dynamics of loop 1 is nonchiral because of the existence of its tail.

We calculated the wave transmissions in the proposed system with $L = 90\,\mu$m and show the x-component electric field distributions in Figs. 3(a)–3(d). Figures 3(a) and 3(b) show the results for counterclockwise loops with a symmetric and antisymmetric mode as the input, respectively, while Figs. 3(c) and 3(d) plot the results for clockwise loops. Since the power flow decays along the waveguiding direction, the field profiles are normalized at each cross section for better readability. We find that for all four cases, the output state

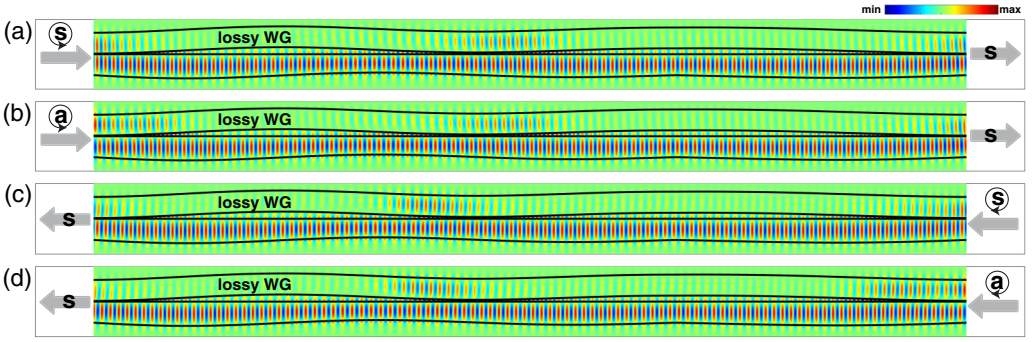

FIG. 3. (a), (b) Numerically simulated x-component electric field distributions along the z axis for counterclockwise loop 1 with (a) symmetric mode and (b) antisymmetric mode being the input eigenmode. (c), (d) Items shown are the same as those in (a), (b) except for clockwise loop 1. The output state is a symmetric mode for all four cases.

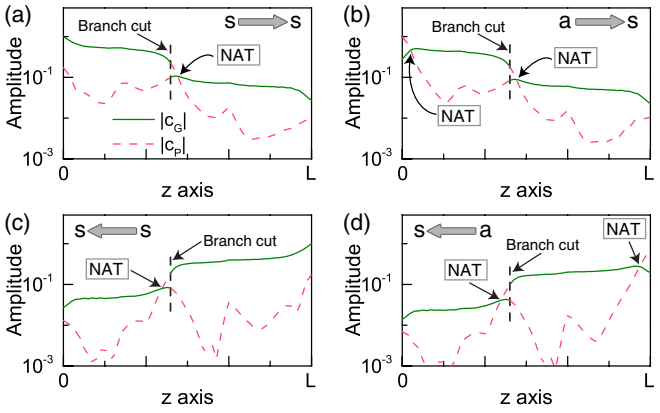

FIG. 4. (a), (b) Calculated amplitudes of the instantaneous eigenmodes along the waveguiding direction for counterclockwise loop 1 with (a) symmetric mode and (b) antisymmetric mode being the input eigenmode. (c), (d) Items shown are the same as those in (a), (b) except for clockwise loop 1.

is always a symmetric mode. This is the phenomenon of nonchiral dynamics; i.e., the output state is independent of the looping direction as well as the symmetry of the input mode. To investigate why the proposed loop exhibits a nonchiral behavior, we project the fields at each cross section (i.e., $x - y$ plane) onto the instantaneous eigenfields and obtain the amplitude coefficient of the two eigenmodes as a function of z. Details of the method can be found in Ref. [34]. We use c_G and c_P to represent, respectively, the amplitude coefficient of the eigenmode on the green sheet and the pink sheet. The results are shown in Figs. 4(a)–4(d) for different encircling directions and different input states. These extracted amplitude coefficients can also be used to draw the trajectory of the eigenmode evolution on the energy sheets. Figures 5(a)–5(d) plot the trajectories on the imaginary part of the Riemann

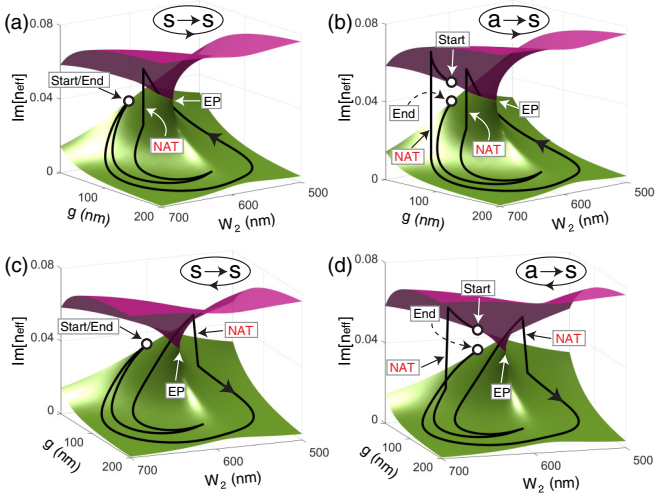

FIG. 5. (a), (b) Trajectories of the state evolution on the imaginary part of the Riemann sheets for counterclockwise loop 1 with (a) symmetric mode and (b) antisymmetric mode being the input eigenmode. (c), (d) Items shown are the same as those in (a), (b) except for clockwise loop 1.

sheets, where the trajectory is marked on the green (pink) sheet when c_G (c_P) dominates the instantaneous state. We will elucidate the complex dynamics in the encircling processes based on the results in Figs. 3–5.

We first consider counterclockwise loops. When the input eigenmode is a symmetric mode, as shown in Fig. 5(a), the starting state lies on the green sheet. One important rule in non-Hermitian systems is that the state is stable only when it evolves on the Riemann sheet with the lowest loss (i.e., the green sheet in our system) [26,27,30]. After encountering the branch cut, the state climbs up to the pink sheet on which it is no longer stable. A nonadiabatic transition (NAT) occurs after some delay time [27,30] and the state jumps back to the green stable sheet. The state then evolves on the green sheet for the rest of the loop and the final state is a symmetric mode lying on the green Riemann sheet. The final state is the same as the input state [also see Fig. 3(a) for field profiles] because of the one NAT. This NAT can also be characterized by the crossing between the two amplitude coefficients in Fig. 4(a). We add a discussion on the aforementioned delay time. In the process of EP encircling, a NAT does not occur immediately when the state begins to evolve on an unstable sheet. It will take a certain time (i.e., the delay time) for the NAT to appear. This delay time can be estimated from numerical simulations. For example, the time span between the branch cut and the NAT in Fig. 4(a) is the delay time. The NAT and the corresponding delay time are related to the losses experienced by the state when it evolves on the unstable sheet (e.g., higher losses can induce a shorter delay time).

Figure 5(b) shows the trajectory with an antisymmetric mode being the input which lies on the pink sheet. In this case, the state is not stable from the beginning so that a first NAT comes after a certain delay time and the state jumps to the stable green sheet. The following process is almost the same as the case with a symmetric input, i.e., the state climbs back to the pink sheet again via the branch cut and a second NAT occurs, leading the final state to be a symmetric mode. We find the phenomenon of state flipping (i.e., an antisymmetric input but a symmetric output) from the field profiles [see Fig. 3(b)] because of two NATs in the encircling process. The results of counterclockwise loops indicate that the final state is in fact independent of the injected mode.

We then study clockwise loops. The trajectories on the Riemann sheets with the symmetric mode and antisymmetric mode being the initial state are plotted in Figs. 5(c) and 5(d), respectively. We find that the dynamical behaviors are similar to those in counterclockwise loops. Specifically, the process with a symmetric initial state has one NAT [compare Figs. 5(c) with 5(a)] while that with an antisymmetric input possesses two NATs [compare Figs. 5(d) with 5(b)]. The final state is still a symmetric mode lying on the green sheet [also see Figs. 3(c) and 3(d) for field profiles]. This is a demonstration of nonchiral dynamics in the sense that the final state for loop 1 in our system is always a symmetric mode, which is regardless of the encircling directions.

We discuss the reason why our loop 1 exhibits nonchiral dynamics but loops in previous works show chiral dynamics, although the starting points of all these loops lie close to the branch cut. Our loop 1 is different from other regular loops in the sense that it has a tail, which is in fact the key to the

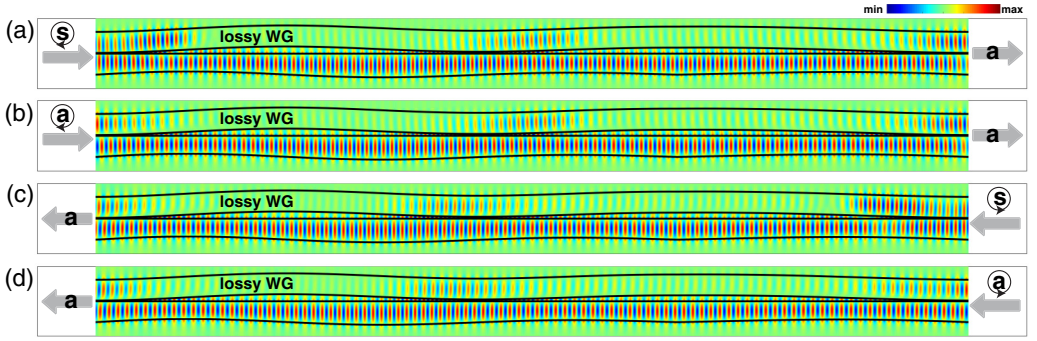

FIG. 6. (a), (b) Numerically simulated x-component electric field distributions along the z axis for clockwise loop 2 with (a) symmetric mode and (b) antisymmetric mode being the input eigenmode. (c), (d) Items shown are the same as those in (a), (b) except for counterclockwise loop 2. The output state is an antisymmetric mode for all four cases.

nonchiral dynamics. When a state is dynamically evolving in a non-Hermitian system, it is not stable when not being on the lowest loss Riemann sheet and NATs would appear after a certain delay time. If the system is sufficiently long (i.e., each possible NAT has enough time to occur), the state should be on the lowest loss sheet when it approaches the end point of the loop. Based on this principle, previous works revealed that for a starting and end point close to the branch cut (or PT-symmetric phase), approaching the end point from different sides of the branch cut will result in different final states because of the topology structure of the energy surface around the EP [10,11,30]. This is the reason why regular loops (e.g., elliptical loops) exhibit chiral dynamics. Applying this principle to our loop 1, we note from Fig. 2(a) that the state for both counterclockwise loop and clockwise loop will approach the end point from the right-hand side of the branch cut, due to the existence of the tail. This same way to approach the end point for counterclockwise and clockwise loops results in the same output state and furthermore the nonchiral dynamics. Our findings indicate that besides the starting and end point of the loop [30], the shape of the loop can also determine the dynamics of the encircling process.

IV. DIFFERENT OUTCOMES FOR HOMOTOPIC LOOPS

We have demonstrated the nonchiral dynamics for loop 1 in the previous section. In this section, we study loop 2 and compare the dynamics of the two loops.

Figures 6(a)–6(d) show the calculated x-component electric field distributions in the system that follows loop 2 in the parameter space for different encircling directions and input states. We find that no matter which eigenmode is injected and in which direction the encircling takes, the final state is always an antisymmetric mode. The corresponding trajectories on the imaginary part of the Riemann sheets for the four cases are plotted in Figs. 7(a)–7(d). For the processes featuring a state flip [i.e., Figs. 7(a) and 7(c)], there are two NATs in the encircling process. In contrast, there is only one NAT for the processes in which the state returns to itself after the loop [i.e., Figs. 7(b) and 7(d)]. For all the four cases, the final state is on the pink sheet.

Although loop 2 also exhibits nonchiral dynamics, its final state (i.e., antisymmetric mode) is different from that of loop 1 (i.e., symmetric mode), as summarized in Table I. This is due to the different locations of the "tails" of the two loops. It can be noted from Figs. 2(a) and 2(b) that the "tail" of loop 1 lies on the right-hand side of the branch cut, while that of loop 2 is located mainly on the left-hand side of the branch cut. As discussed in Sec. III, moving towards the end point from different sides of the branch cut leads to different final states. Therefore, the outcomes of loop 1 and loop 2 are different.

In fact, loop 1 and loop 2 are homotopic loops; i.e., they share the same starting point and one loop can be transformed continuously into another one without crossing any singularity (i.e., the EP) in the parameter space. Homotopic loops have been studied recently in the case of stroboscopic encircling of the EP in which the process is always adiabatic [22,23]. It was proved that for homotopic loops, once the starting state and the encircling direction are the same, the final state must be the same [22]. Our results in this work show that the above conclusion is not applicable to the case of dynamical encircling in which the adiabaticity may break down. Specifically, loop 1 and loop 2 are homotopic loops, but even if the starting state and the encircling direction are the same, the outcomes are completely different.

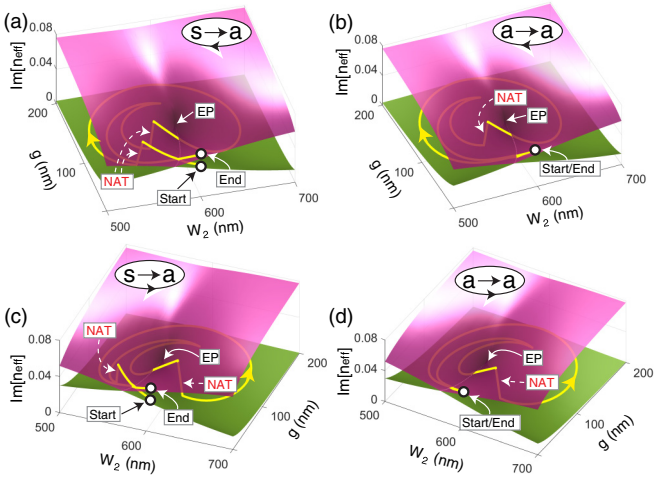

FIG. 7. (a), (b) Trajectories of the state evolution on the imaginary part of the Riemann sheets for clockwise loop 2 with (a) symmetric mode and (b) antisymmetric mode being the input eigenmode. (c), (d) Items shown are the same as those in (a), (b) except for counterclockwise loop 2.

TABLE I. Comparison of the dynamical process of the four loops. Each loop exhibits nonchiral dynamics. Loop 1 and loop 2 are homotopic loops but their outcomes are different. The same behaviors can also be found for loop A and loop B.

Loop	Dynamics	End state of counterclockwise loops	End state of clockwise loops
Loop 1	Nonchiral	Symmetric mode	Symmetric mode
Loop 2	Nonchiral	Antisymmetric mode	Antisymmetric mode
Loop A	Nonchiral	$\|\psi_2\rangle$	$\|\psi_2\rangle$
Loop B	Nonchiral	$\|\psi_1\rangle$	$\|\psi_1\rangle$

V. THEORETICAL DEMONSTRATION OF THE DYNAMICS

We propose an analytical theory to explain the phenomenon associated with homotopic loops. We study a two-state system which is governed by

$$i\partial_t|\psi(t)\rangle = H(t)|\psi(t)\rangle, \tag{3}$$

where $|\psi(t)\rangle = [a(t), b(t)]^T$ is defined to be the time-dependent state vector, and $H(t)$ is the time-dependent Hamiltonian with the form

$$H(t) = \begin{bmatrix} ig(t)+\delta(t) & -1 \\ -1 & -ig(t)-\delta(t) \end{bmatrix}. \tag{4}$$

The system is PT symmetric when $\delta = 0$. We consider a $g-\delta$ parameter space in which a pair of EPs reside at $g = \pm 1$ and $\delta = 0$. In the following study, we focus on the EP at $g = 1$ and $\delta = 0$. The parameter space with this EP is shown in Figs. 8(a) and 8(b), where we generate two homotopic loops, i.e., loop A and loop B. The EP is marked by the star, and the PT-symmetric phase and PT-broken phase are marked by the red dashed line and red dotted line, respectively. The starting and end points of the two loops lies exactly in the PT-symmetric phase so that the dynamical behavior of them should be the same as that of loop 1 and loop 2 studied in Secs. III and IV. Therefore, loop A and loop B are good candidates to study why homotopic loops show distinct dynamical behaviors.

Figure 8(a) shows a common point for clockwise and counterclockwise loop A that when approaching the end point, the state will travel from the PT-broken phase to the PT-symmetric phase in a clockwise direction for both loops (see the blue dashed curve for counterclockwise loop A and the blue dash-dotted curve for clockwise loop A). For loop B, on the contrary, we find in Fig. 8(b) that the state will travel counterclockwise for both counterclockwise loop B (see the green dash-dotted curve) and clockwise loop B (see the green dashed curve) when approaching the end point of the loop. Such difference is in fact the key reason for the different dynamics of loop A and loop B. We will prove that when a state starts from the PT-broken phase and ends at the PT-symmetric phase, the final states are different for clockwise trajectory and counterclockwise trajectory, and the results are independent of the input state.

To prove this point, we consider two trajectories, namely, trajectory A and trajectory B in Fig. 8(c), with the starting point and end point lying in the PT-broken phase and PT-symmetric phase, respectively. The trajectories follow the expression $g(t) = 1-\rho\cos(\gamma t)$ and $\delta(t) = \rho\sin(\gamma t)$, where ρ is the radius and γ measures the adiabaticity of the process. We have $t = t_0 = -\pi/|\gamma|$ and $t = t_{\rm end} = 0$, respectively, at the starting point and the end point. Trajectory A is generated by a negative γ while a positive γ leads to trajectory B. At the starting point, the two eigenvalues are $\lambda_{\rm G} = i\sqrt{\rho^2+2\rho}$ and $\lambda_{\rm L} = -i\sqrt{\rho^2+2\rho}$, respectively, corresponding to a gain state and a loss state. Their corresponding eigenvectors are $|\psi_{\rm G}\rangle = [1, i(\rho+1-\sqrt{\rho^2+2\rho})]^T$ and $|\psi_{\rm L}\rangle = [1, i(\rho+1+\sqrt{\rho^2+2\rho})]^T$. At the end point, on the contrary, the two eigenstates lie in the PT-symmetric phase with eigenvalues $\lambda_1 = \cos\theta$ and $\lambda_2 = -\cos\theta$, and eigenvectors $|\psi_1\rangle = [1, e^{i\theta}]^T$ and $|\psi_2\rangle = [1, -e^{-i\theta}]^T$, where $\theta = \arcsin(1-\rho)$.

We first solve Eq. (3) numerically along trajectory A ($\gamma = -0.01$) and trajectory B ($\gamma = 0.01$). We calculate the ratio of the two elements of the state vector at the end point [i.e., $b(t_{\rm end})/a(t_{\rm end})$] as a function of ρ, which can be used to recognize the symmetry of the final state (i.e., $|\psi_1\rangle$ or $|\psi_2\rangle$). The results for trajectory A are shown by solid lines in Figs. 9(a) and 9(b), where the initial state is a gain state

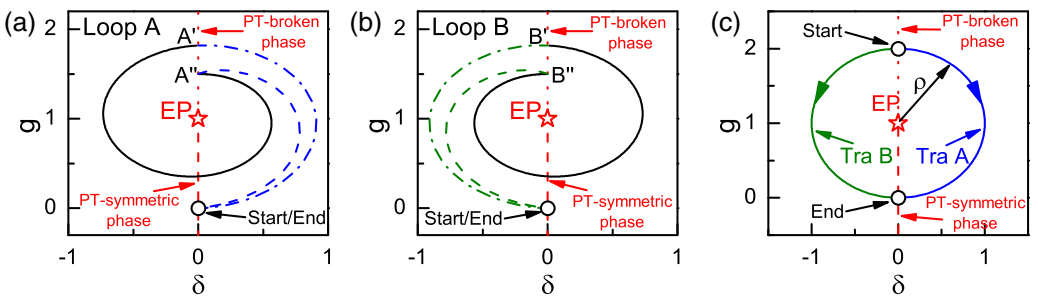

FIG. 8. (a), (b) $g-\delta$ parameter space in which an EP resides at $g = 1$ and $\delta = 0$. (a) Loop A and (b) loop B that encircles the EP with the starting and end point (see the circle) in the PT-symmetric phase. (c) Trajectories A and B with the starting point and end point lying in the PT-broken phase and PT-symmetric phase, respectively.

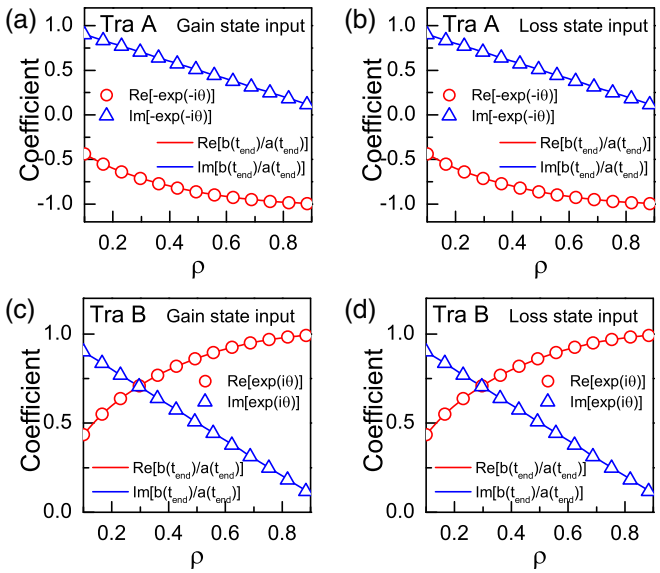

FIG. 9. (a), (b) Calculated $b(t_{\rm end})/a(t_{\rm end})$ (solid lines) as a function of ρ for trajectory A with (a) a gain state and (b) a loss state being the initial state. The symbols show the values of $-\exp(-i\theta)$. (c), (d) Items shown are the same as those in (a), (b) except for trajectory B (solid lines) and $\exp(i\theta)$ (symbols).

$|\psi_{\rm G}\rangle$ and a loss state $|\psi_{\rm L}\rangle$, respectively. We find that along trajectory A, the initial state makes no difference to the final state, since Figs. 9(a) and 9(b) look the same. We also plot the values of $-\exp(-i\theta)$ as a function of ρ [see the symbols in Figs. 9(a) and 9(b)], which match well with the values of $b(t_{\rm end})/a(t_{\rm end})$, indicating that the final state is $|\psi_2\rangle = [1, -e^{-i\theta}]^T$. In the same way, Figs. 9(c) and 9(d) plot the results for trajectory B (solid lines) and the values of $\exp(i\theta)$ (symbols), demonstrating that the final state along trajectory B is always $|\psi_1\rangle = [1, e^{i\theta}]^T$, regardless of the initial state.

We now theoretically derive the final states of trajectories A and B. Equations (3) and (4) can be recast into second-order differential equations for $a(t)$ and $b(t)$, e.g., $d^2a(t)/dt^2 - [\rho^2 e^{2i\gamma t} - \rho(2+i\gamma)e^{i\gamma t}]a(t) = 0$. Exact solutions of the dynamical processes were first obtained by Berry and Uzdin [25]. Following their idea [25] as well as the method used in Refs. [28,30], the above equation can be reduced into a degenerate hypergeometric differential equation, and the solutions are confluent hypergeometric functions of the first kind F and second kind U. We first consider trajectory B with $\gamma > 0$, where the starting point lies in the PT-broken phase. It was derived in Ref. [30] that the state vector at the final time step $t_{\rm end} = 0$ can be related to the initial state at $t_0 = -\pi/\gamma$ via a transfer matrix,

$$[a(t_{\rm end}), b(t_{\rm end})]^T = \sigma(t_{\rm end}) M_1(t_{\rm end}) M_2 M_3 [a(t_0), b(t_0)]^T, \tag{5}$$

where the matrix elements are

$$M_1(t_{\rm end}) = \begin{bmatrix} F^{(0)}_{t=0} & U^{(0)}_{t=0} \\ iF^{(0)}_{t=0} + 2\rho e^{i\gamma t} F^{(1)}_{t=0}/\gamma & iU^{(0)}_{t=0} - 2\rho e^{i\gamma t} U^{(1)}_{t=0}/\gamma \end{bmatrix}, \tag{6a}$$

$$M_2 = \begin{bmatrix} \rho U^{(0)}_{t=-\pi/\gamma}/\gamma + 2i\rho U^{(1)}_{t=-\pi/\gamma}/\gamma^2 & -U^{(0)}_{t=-\pi/\gamma} \\ -\rho F^{(0)}_{t=-\pi/\gamma}/\gamma + 2i\rho F^{(1)}_{t=-\pi/\gamma}/\gamma^2 & F^{(0)}_{t=-\pi/\gamma} \end{bmatrix}, \tag{6b}$$

$$M_3 = \begin{bmatrix} 1 & 0 \\ (1+\rho)/\gamma & i/\gamma \end{bmatrix}, \tag{6c}$$

with $F^{(n)}$ and $U^{(n)}$ being confluent hypergeometric functions [36] $F(n+i/\gamma, n+1, -2i\rho e^{i\gamma t}/\gamma)$ and $U(n+i/\gamma, n+1, -2i\rho e^{i\gamma t}/\gamma)$, respectively, and $\sigma(t_{\rm end}) = i\Gamma(i/\gamma)$ where Γ is the gamma function. We further define $M = M_1(t_{\rm end}) M_2 M_3 = \left[\begin{smallmatrix} m_{11} & m_{12} \\ m_{21} & m_{22} \end{smallmatrix}\right]$, and the final state satisfies

$$b(t_{\rm end})/a(t_{\rm end}) = \frac{m_{21} a(t_0) + m_{22} b(t_0)}{m_{11} a(t_0) + m_{12} b(t_0)}. \tag{7}$$

The key to solving Eq. (7) is to derive the elements of matrix M, which are

$$m_{11} = \frac{1}{\gamma}\left(U^{(0)}_{t=0} F^{(0)}_{t=-\pi/\gamma} - F^{(0)}_{t=0} U^{(0)}_{t=-\pi/\gamma}\right) + \frac{2i\rho}{\gamma^2}\left(F^{(0)}_{t=0} U^{(1)}_{t=-\pi/\gamma} + U^{(0)}_{t=0} F^{(1)}_{t=-\pi/\gamma}\right), \tag{8a}$$

$$m_{12} = \frac{i}{\gamma}\left(U^{(0)}_{t=0} F^{(0)}_{t=-\pi/\gamma} - F^{(0)}_{t=0} U^{(0)}_{t=-\pi/\gamma}\right), \tag{8b}$$

$$\begin{aligned} m_{21} = &-\frac{2\rho}{\gamma^2}\left(F^{(0)}_{t=0} U^{(1)}_{t=-\pi/\gamma} + U^{(0)}_{t=0} F^{(1)}_{t=-\pi/\gamma}\right) + \frac{4i\rho^2}{\gamma^3}\left(F^{(1)}_{t=0} U^{(1)}_{t=-\pi/\gamma} - U^{(1)}_{t=0} F^{(1)}_{t=-\pi/\gamma}\right) \\ &- \frac{i}{\gamma}\left(F^{(0)}_{t=0} U^{(0)}_{t=-\pi/\gamma} - U^{(0)}_{t=0} F^{(0)}_{t=-\pi/\gamma}\right) - \frac{2\rho}{\gamma^2}\left(F^{(1)}_{t=0} U^{(0)}_{t=-\pi/\gamma} + U^{(1)}_{t=0} F^{(0)}_{t=-\pi/\gamma}\right), \end{aligned} \tag{8c}$$

$$m_{22} = \frac{1}{\gamma}\left(F^{(0)}_{t=0} U^{(0)}_{t=-\pi/\gamma} - U^{(0)}_{t=0} F^{(0)}_{t=-\pi/\gamma}\right) - \frac{2i\rho}{\gamma^2}\left(F^{(1)}_{t=0} U^{(0)}_{t=-\pi/\gamma} + U^{(1)}_{t=0} F^{(0)}_{t=-\pi/\gamma}\right). \tag{8d}$$

In the limit of $\gamma \to 0$, the values of $F^{(0)}_{t=-\pi/\gamma}$, $F^{(1)}_{t=-\pi/\gamma}$, $U^{(0)}_{t=0}$, and $U^{(1)}_{t=0}$ are considerably smaller than $F^{(0)}_{t=0}$, $F^{(1)}_{t=0}$, $U^{(0)}_{t=-\pi/\gamma}$, and $U^{(1)}_{t=-\pi/\gamma}$. Using these approximations, it can then be derived that

$$\frac{m_{22}}{m_{12}} = \frac{m_{21}}{m_{11}} = i + \frac{2\rho}{\gamma}\frac{F^{(1)}_{t=0}}{F^{(0)}_{t=0}}. \tag{9}$$

It was proved in Ref. [28] using the asymptotic expressions of the hypergeometric functions that $F^{(1)}_{t=0}/F^{(0)}_{t=0} = \gamma(e^{i\theta} - i)/(2\rho)$. Inserting this expression into Eqs. (7) and (9), we obtain

$$b(t_{\text{end}})/a(t_{\text{end}}) = e^{i\theta}, \tag{10}$$

which indicates that the final state of trajectory B is always $|\psi_1\rangle = [1, e^{i\theta}]^T$ and independent of the initial state $|\psi(t_0)\rangle$.

The dynamics of trajectory A can be studied based on the principle that the final state (a, b) would become $(a^*, -b^*)$ when the sign of γ is flipped [28]. We then find that the final state of trajectory A is $|\psi_2\rangle = [1, -e^{-i\theta}]^T$.

The mode switching behaviors of trajectory A and trajectory B can be employed to explain the different outcomes of loop A and loop B. We note from Fig. 8 that trajectory $A(B)$ is the final part of loop $A(B)$ for both clockwise and counterclockwise cases. Consider a state that travels along loop $A(B)$. No matter which eigenstate is injected at the starting point and in which direction the encircling takes, the instantaneous state must be a combination of $|\psi_{\text{G}}\rangle$ and $|\psi_{\text{L}}\rangle$ when it reaches the starting point of trajectory $A(B)$ [see points A' and A'' in Fig. 8(a), and points B' and B'' in Fig. 8(b)]. We have proved that the final state of trajectory $A(B)$ does not depend on the initial state. Therefore, the outcome of loop $A(B)$ is the same as that of trajectory $A(B)$; i.e., the final state of loop A is $|\psi_2\rangle$ while that of loop B is $|\psi_1\rangle$, which is independent of the initial state as well as the encircling direction. The mode switching behaviors of loop A and loop B are summarized in Table I. The different outcomes for these two homotopic loops are due to the fact that when a state travels from the PT-broken phase to the PT-symmetric phase, different encircling directions result in different final states.

VI. CONCLUSION

In summary, we have found unexpected phenomena and revealed some unique physics in the process of dynamically encircling EPs in non-Hermitian systems. We showed that the mode switching behaviors do not depend on homotopy, i.e., the outcomes can be different even if two homotopic loops share the same starting state and the EP enclosed is encircled in the same direction (e.g., loop 1 and loop 2). A complementary phenomenon to this is that the mode switching behaviors can be the same for nonhomotopic loops. For example, it was found in Ref. [31] that the chiral dynamics can also occur even if the loop excludes any EP, where the loop is obviously not homotopic to the loop enclosing an EP. These examples indicate that the consequence in the process of dynamically encircling EPs is very different from that of stroboscopic encircling, where homotopy plays a key role in determining the mode switching behaviors. We further studied the key factors to determine the mode switching behavior in the case of dynamic encircling. We note from previous studies that the location of the starting point can determine the dynamics, i.e., a starting point lying somewhere where two eigenmodes share almost the same loss (e.g., the branch cut or PT-symmetric phase) can result in a chiral mode switching behavior [10,11,24,28,31], whereas the dynamics is nonchiral if there is only one eigenmode exhibiting the lowest loss at the starting point (e.g., the PT-broken phase) [30]. We gave a counterexample to this conclusion using loop 1 and loop 2 that have a tail. We showed that the dynamics can be nonchiral even if the starting point lies close to the branch cut. This adds to our understanding of the case of dynamical encircling; i.e., besides the starting point of the loop, the trajectory along which the state approaches the end point can also determine the mode switching behavior. These phenomena and physics may find applications for the design of alternative wave manipulation strategies in non-Hermitian systems.

ACKNOWLEDGMENTS

This work was supported by the National Natural Science Foundation of China (Grants No. 61605056, No. 61590930 and No. 61435005) and the China Postdoctoral Science Foundation (Grant No. 2016M591480). C.T.C. was also supported by the Hong Kong Research Grants Council through Grant No. AoE/P-02/12.

[1] I. Rotter, J. Phys. A **42**, 153001 (2009).
[2] N. Moiseyev, *Non-Hermitian Quantum Mechanics* (Cambridge University Press, Cambridge, 2011).
[3] W. D. Heiss, J. Phys. A **45**, 444016 (2012).
[4] A. Guo, G. J. Salamo, D. Duchesne, R. Morandotti, M. Volatier-Ravat, V. Aimez, G. A. Siviloglou, and D. N. Christodoulides, Phys. Rev. Lett. **103**, 093902 (2009).
[5] W. Chen, S. K. Özdemir, G. Zhao, J. Wiersig, and L. Yang, Nature **548**, 192 (2017).
[6] H. Hodaei, A. U. Hassan, S. Wittek, H. Garcia-Gracia, R. El-Ganainy, D. N. Christodoulides, and M. Khajavikhan, Nature **548**, 187 (2017).
[7] B. Peng, S. K. Özdemir, S. Rotter, H. Yilmaz, M. Liertzer, F. Monifi, C. M. Bender, F. Nori, and L. Yang, Science **346**, 328 (2014).
[8] L. Feng, Z. J. Wong, R. M. Ma, Y. Wang, and X. Zhang, Science **346**, 972 (2014).
[9] H. Hodaei, M. Miri, M. Heinrich, D. N. Christodoulides, and M. Khajavikhan, Science **346**, 975 (2014).
[10] J. Doppler, A. A. Mailybaev, J. Böhm, U. Kuhl, A. Girschik, F. Libisch, T. J. Milburn, P. Rabl, N. Moiseyev, and S. Rotter, Nature **537**, 76 (2016).
[11] J. W. Yoon, Y. Choi, C. Hahn, G. Kim, S. H. Song, K. Y. Yang, J. Y. Lee, Y. Kim, C. S. Lee, J. K. Shin, H. S. Lee, and P. Berini, Nature **562**, 86 (2018).
[12] Y. D. Chong, L. Ge, and A. D. Stone, Phys. Rev. Lett. **106**, 093902 (2011).
[13] A. Regensburger, C. Bersch, M. Miri, G. Onishchukov, D. N. Christodoulides, and U. Peschel, Nature **488**, 167 (2012).

[14] H. Xu, D. Mason, L. Jiang, and J. G. E. Harris, Nature **537**, 80 (2016).
[15] X. L. Zhang, S. B. Wang, W. J. Chen, and C. T. Chan, Phys. Rev. A **96**, 022112 (2017).
[16] X. L. Zhang, X. B. Wang, and C. T. Chan, Phys. Rev. Appl. **10**, 034045 (2018).
[17] W. D. Heiss, Phys. Rev. E **61**, 929 (2000).
[18] C. Dembowski, H.-D. Gräf, H. L. Harney, A. Heine, W. D. Heiss, H. Rehfeld, and A. Richter, Phys. Rev. Lett. **86**, 787 (2001).
[19] T. Gao, E. Estrecho, K. Y. Bliokh, T. C. H. Liew, M. D. Fraser, S. Brodbeck, M. Kamp, C. Schneider, S. Höfling, Y. Yamamoto, F. Nori, Y. S. Kivshar, A. G. Truscott, R. G. Dall, and E. A. Ostrovskaya, Nature **526**, 554 (2015).
[20] K. Ding, G. Ma, M. Xiao, Z. Q. Zhang, and C. T. Chan, Phys. Rev. X **6**, 021007 (2016).
[21] W. D. Heiss and G. Wunner, Eur. Phys. J. D **71**, 312 (2017).
[22] Q. Zhong, M. Khajavikhan, D. N. Christodoulides, and R. El-Ganainy, Nat. Commun. **9**, 4808 (2018).
[23] E. J. Pap, D. Boer, and H. Waalkens, Phys. Rev. A **98**, 023818 (2018).
[24] R. Uzdin, A. Mailybaev, and N. Moiseyev, J. Phys. A: Math. Theor. **44**, 435302 (2011).
[25] M. V. Berry and R. Uzdin, J. Phys. A: Math. Theor. **44**, 435303 (2011).
[26] I. Gilary, A. A. Mailybaev, and N. Moiseyev, Phys. Rev. A **88**, 010102(R) (2013).
[27] T. J. Milburn, J. Doppler, C. A. Holmes, S. Portolan, S. Rotter, and P. Rabl, Phys. Rev. A **92**, 052124 (2015).
[28] A. U. Hassan, B. Zhen, M. Soljačić, M. Khajavikhan, and D. N. Christodoulides, Phys. Rev. Lett. **118**, 093002 (2017).
[29] Y. Choi, C. Hahn, J. W. Yoon, S. H. Song, and P. Berini, Nat. Commun. **8**, 14154 (2017).
[30] X. L. Zhang, S. B. Wang, B. Hou, and C. T. Chan, Phys. Rev. X **8**, 021066 (2018).
[31] A. U. Hassan, G. L. Galmiche, G. Harari, P. LiKamWa, M. Khajavikhan, M. Segev, and D. N. Christodoulides, Phys. Rev. A **96**, 052129 (2017).
[32] H. Wang, L. J. Lang, and Y. D. Chong, Phys. Rev. A **98**, 012119 (2018).
[33] X. L. Zhang and C. T. Chan, Phys. Rev. A **98**, 033810 (2018).
[34] X. L. Zhang, T. Jiang, H. B. Sun, and C. T. Chan, arXiv:1806.07649.
[35] www.comsol.com.
[36] L. J. Slater, *Confluent Hypergeometric Functions* (Cambridge University Press, Cambridge, UK, 1960).